Exploring the impact of Bond-Dilution on Magnetic properties of a mixed spin-1 and spin-3/2 cylindrical Ising Nanotube: Effective Field Theory

L. Darbali[1], K. Htoutou[1,2], B. Nmaila[1], L. B. Drissi[1,3,4], R.AhlLaamara[1,3].

1-LPHE-MS, Laboratory of High Energy Physics-Modeling & Simulations,

Department of Physics, Faculty of Science, Mohammed V University in Rabat, Morocco,

2-CRMEF, Department of Physics, Regional Center for Education and Training Professions, Fes-Meknes, Morocco, *

3-CPM, Center of Physics and Mathematics, Faculty of Science, Mohammed V University in Rabat, Morocco and

4-Hassan II Academy of Sciences and Technology, Rabat, Morocco

Abstract

The magnetic properties of Ising-diluted nanotubes with mixed spin-$(1/2, 3/2)$ and cylindrical core-shell structures are studied using effective field theory and probability distribution technique. This framework is focused on exploring the effects of the bond disorder in the core and the shell sublattices, on the magnetic and thermodynamic properties of the system, such as the total longitudinal magnetization, the internal energy, the free energy, and the magnetic susceptibility, as well as the hysteresis multi-loop behaviors.

Depending on the longitudinal crystal fields of the core (D_c) and the shell (D_s) sublattices, and of the exchange coupling core-shell R_{cs}, our result contains several interesting phenomena such as the second-order phase transitions, and the existence of $N-$, $Q-$, $P-$, $R-$ and $S-$ type compensation behaviors according to Neel's and Strecka's theories of ferrimagnetism. Moreover, the system presents a quintuple hysteresis loop phenomenon for total magnetization under certain values of D_c, T, and R_{cs}.

Keywords: Effective field theory, Probability distribution technique, Ferrimagnetic, Ising model, Cylindrical core-shell structure, diluted nanotube, Compensation behaviors, Hysteresis behavior, Multi-loops behavior, thermodynamic functions.

*Corresponding author:khadija.htoutou2021@gmail.com

1. INTRODUCTION

Recently, magnetic nanostructures, including nanowires, nanoparticles, nanorods, nanofibers, and nanotubes, have been the focus of extensive experimental and theoretical research due to their distinct properties compared to conventional materials and their potential applications in miniaturized devices. Particularly, nanotubes have attracted more attention since their discovery by Ijima in 1991 [1]. Due to their potential applications in various domains, including electronics, optics, mechanics, and even biology, many researchers have dedicated their studies to nanotube research [2–6]. Especially, cylindrical nanotubes with a core-shell structure have gradually become an important type of functional material.

From the experimental opinion, many efforts have been devoted to fabricating various core-shell nanotubes, for example, $Co-Ni$ nanotubes [7–11]. With the intention of obtaining the SnO_2 nanotube in controllable form, Ye used one-dimensional mesoporous SiO_2 as an effective template by the hydrothermal method. The results show that the SnO_2 nanotubes have better performance than the ordinary SnO_2 nanoparticles, used as the anode material in the lithium ion battery [12]. Also D. Zhou et al. prepared a series of $FeNi$ magnetic nanotubes by using the pore wetting template method [13].

On the other hand, theoretical research can provide more reasonable explanations for experimental results. Different theoretical methods are used to understand the magnetic properties of these core-shell nanotubes, including the mean field theory (MFT) [14], Monte Carlo (MC) simulations [15–17], effective field theory (EFT) [18–20], and others. Due to the simplicity and practicability of Ising models, this kind of material can be well described by mixed-spin Ising systems.

One of the most interesting properties of ferrimagnetic nanomaterials is the existence of compensation temperature, which is of great importance in applications of thermal magnetic recording [21–25]. In this sense, T. Kaneyoshi has investigated magnetic properties, critical and compensation temperatures in a cylindrical Ising nanowire (or nanotube) with a negative interlayer coupling at the surface by using both the effective-field theory with correlations and the shell-core concept [7, 26, 28]. Moreover, quintuple and triple hysteresis loops have been observed respectively in core-shell Ising nanotube and molecular-based magnetic materials through Monte Carlo (MC) simulations [29, 30]. The hysteresis characteristics of core-shell magnetic nanostructures have similarly been examined using EFT with correlations [31, 32]. These triple loops typically emerge at low temperatures, influenced by several factors such as magnetic and crystal fields, temperature, and ferrimagnetic exchange coupling [33]. This phenomenon holds significant potential for applications in multi-state memory devices [34, 35].

Several theoretical and numerical methods are intended to study magnetic and thermodynamic properties of various ferrimagnetic mixed spin systems like $(1, 1/2)$ [36–38], $(1, 3/2)$[39, 40], $(2, 3/2)$ [41], and $(3/2, 5/2)$ [42, 43]. Among these methods, we find the Effective-Field Theory with correlations (EFT) [44, 45], the Mean-Field Approximation (MFA) [46, 47], the Monte Carlo Simulation (MCS) [48, 49], the Glauber-Type Stochastic Dynamics Approach based on the effective-field theory [50], the Blume–Capel Method [51], the Dynamic Effective-Field Theory (DEFT) [52], and the Green's Function Technique [53].

The mixed-spin (1,3/2) system is considered one of the most popular mixed systems, because it can be qualified as a suitable model for magnetic nanomaterials. Thus, experimentally, J. Y. Chen et al. have synthesized Ni and $Co - NiO - Ni$ core-shell nanotube arrays by a simple template-assisted direct electro-deposition method [54]. Also, a series of $CoxNi1 - x$ (x = 0–0.5) nanotubes have been successfully prepared by electrodeposition Method [55].

From the theoretical point of view, this kind of nanotube can be well described by the mixed-spin $(1, 3/2)$ system. In addition, the mixed-spin $(1, 3/2)$ Ising models have been developed by different numerical methods for understanding the equilibrium behaviors in statistical physics. Jiang et al. have proposed a metallic nanotube that consists of the ferromagnetic spin-$3/2$ inner shell and spin-1 outer shell. The effects of the ferrimagnetic interlayer coupling, the anisotropy and the transverse field on magnetic and thermodynamics are studied by using the EFT [56]. A. Arbaoui, K.Htoutou et al. have treated the reentrant phenomena characterizing first order phase transitions, and the exchange bias effect manifested by asymmetric hysteresis loops for a core–shell nanotube with mixed spin $(1, 3/2)$ by combining both the effective field theory and the probability distribution technique [57]. Y. Benhouria et al. have studied the dynamic behavior of a ferromagnetic or ferrimagnetic double-wall nanotube with mixed-spin $(1, 3/2)$ system by using the dynamic MC simulation [58]. Liang et al. have investigated the magnetization, the internal energy, the initial susceptibility, and the specific heat of a double-wall cubic metal nanotube, which consists of the ferromagnetic spin-1 inner shell and spin-3/2 surface shell in the presence of both the single-ion anisotropy and transverse field by EET with correlations [59]. In particular, the effects of various physical parameters, such as the single-ion anisotropies and exchange couplings, on magnetization, the susceptibility, the internal energy, the specific heat, and the hysteresis loop of the system also require further discussion. However, we devoted a previous work to study the effect of bond dilution in both core and surface layers of an Ising mixed spins $(1/2, 3/2)$ nanotube to investigate the discussed properties [33]. Therefore, the current work represents a continuation of the last study, which consisted of evaluating the behavior of the system by increasing the spin. The paper is divided into three parts; the first is devoted to the model and formalism of the effective field theory in question, the second to the results and discussion, and the third to the conclusion.

2. MODEL AND FORMALISM

We consider a core-shell nanotube, composed of a ferromagnetic core of spin $\sigma = \frac{3}{2}$, surrounded by a surface layer of spin $S = 1$ (Figure 1).

The Hamiltonian describing this system, introducing only the summation over the first nearest neighbors, is given by the following model:

$$H = -J_c \sum_{<ij>} \sigma_{iz}^c \sigma_{jz}^c - J_s \sum_{<kl>} S_{kz}^s S_{lz}^s - J_{cs} \sum_{<ik>} \sigma_{iz}^c S_{kz}^s - D_z^{(c)} \sum_{i\in(c)} (\sigma_{iz})^2 - D_z^{(s)} \sum_{k\in(s)} (S_{kz})^2 , \tag{1}$$

Where σ_{iz} denotes the z-component of a $\frac{3}{2}$ quantum spin at site i, S_{kz} denotes the z-component of an 1 quantum spin at site k, and D_c and D_s are the uniaxial anisotropies relative to the core and shell, respectively.

J_c and J_s are the ferromagnetic spin-spin exchange interaction couplings of the core and shell, respectively, and J_{cs} is the ferrimagnetic core-shell exchange interaction coupling.

The bond dilution is described by a random distribution of exchange interactions governed by the following probability law

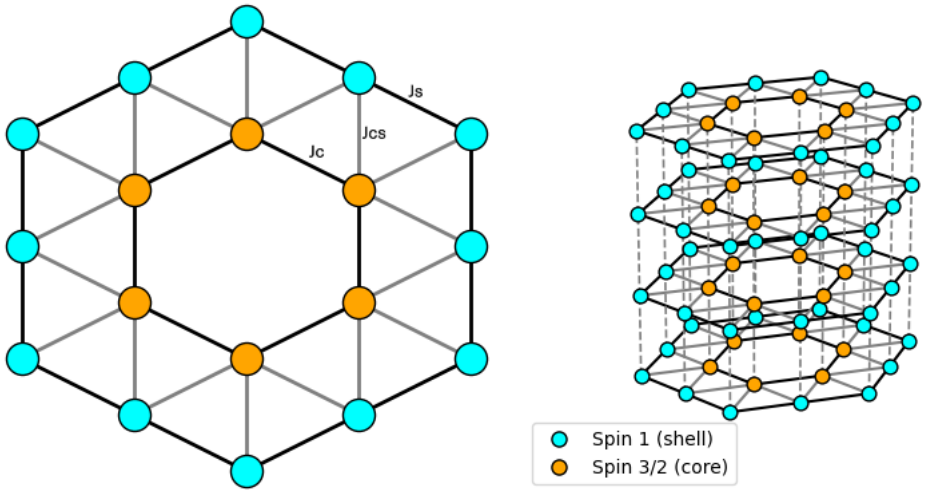

FIG. 1: Cross section of a cylindrical nanotube with a core-shell structure, the atoms in red with spin $\sigma = 3/2$ constitute the core and the atoms with spin $S = 1$ in blue constitute the shell, where the atoms of the last layer of the core have a ferrimagnetic coupling to those of the shell.

[32] :

$$P\left(J_{ij}^{c}\right) = p\delta\left(J_{ij}^{c}\right) + (1-p)\,\delta\left(J_{ij}^{c} - J_{c}\right). \qquad P\left(J_{ij}^{s}\right) = q\delta\left(J_{ij}^{s}\right) + (1-q)\,\delta\left(J_{ij}^{s} - J_{s}\right). \tag{2}$$

where: $0 \leq p \leq 1$ and $0 \leq q \leq 1$, p and q indicate the bond concentrations.

For the core, we have only one type of site. Each is surrounded by two spin neighbors $\sigma = \frac{3}{2}$ ($N^{c} = 2$), and three spin neighbors ($S = 1$), but not of the same type ($N^{s,1} = 1, N^{s,2} = 2$).

The same applies to the shell's sites, $(H_0^s)_\alpha$ denotes the Hamiltonian of a single shell's site, it is indexed by α and it is obvious that we have two types of sites in the surface, the first with a single spin neighbors $\sigma = \frac{3}{2}$ ($N_1^c = 1$) and two spin neighbors $S = 1$ ($N_1^s = 2$), the second type with two spin $\sigma = \frac{3}{2}$ ($N_2^c = 2$) and two spin $S = 1$ ($N_2^s = 2$).

The method used consists of focusing the attention on a central site 0, and the neighboring sites with which it directly interacts. Therefore, the Hamiltonians at a single site are given by :

$$H_0^c = -X^c \sigma_{0z}^c - Y^c \left(\sigma_{0z}^c\right)^2 \quad \text{and} \quad (H_0^s)_\alpha = -X_\alpha^s S_{0z}^s - Y^s \left(S_{0z}^s\right)^2, \tag{3}$$

For the core sites we have:

$$X^c(S_k, \sigma_j) = J_c \sum_{j=1}^{N^c} \sigma_{jz}^c + J_{cs} \sum_{k=1}^{N^s} S_{kz}^s \quad , \quad Y^c = D^c$$

and for the shell ones we have:

$$\begin{array}{l} X_1^s(S_l,\sigma_i) = \ J_{cs}\sum\limits_{i=1}^{N_1^c}\sigma_{iz} + J_s\sum\limits_{l=1}^{N_1^s} S_{lz}^s \ , \\ X_2^s(S_l,\sigma_i) = \ J_{cs}\sum\limits_{i=1}^{N_2^c}\sigma_{iz} + J_s\sum\limits_{l=1}^{N_2^s} S_{lz}^s \ , \end{array} \quad \text{and} \ \ Y^s = D^s$$

We will determine the expressions for the magnetizations $m_s = \langle S_i \rangle$ and $m_c = \langle \sigma_k \rangle$, the quadratic moment $q_s = \langle \langle S_i \rangle^2 \rangle$ and $q_c = \langle \langle \sigma_k \rangle^2 \rangle$ and the moment $r_c = \langle \langle \sigma_k \rangle^3 \rangle$, in the case where the system has a bonding disorder. According to the effective field theory, we have :

$$\langle (S_i^z)^p \rangle = \langle F^p(X', Y') \rangle = \langle \frac{Tr_0[exp(-\beta(H_0^s)_\alpha)(S_i^z)^p]}{Tr_0[exp(-\beta(H_0^s)_\alpha)]} \rangle \qquad ; \qquad 1 \leq p \leq 2S \tag{4}$$

$$\langle (\sigma_i^z)^n \rangle = \langle F^n(X, Y) \rangle = \langle \frac{Tr_0[exp(-\beta H_0^c)(\sigma_i^z)^n]}{Tr_0[exp(-\beta H_0^c)]} \rangle \qquad ; \qquad 1 \leq n \leq 2S \tag{5}$$

where $\beta = \frac{1}{K_B T}$ and K_B is Boltzmann's constant and T is the absolute temperature.

Then, for the shell, we have:

$$\begin{cases} (m_{sz})_\alpha \ = \ \langle S_i^z \rangle = \langle G(X_\alpha^s, Y^s) \rangle \\ (q_{sz})_\alpha \ = \ \langle (S_i^z)^2 \rangle = \langle H(X_\alpha^s, Y^s) \rangle \end{cases} \tag{6}$$

and for the core, we have:

$$\begin{cases} m_{cz} \ = \ \langle \sigma_i^z \rangle = \langle F_1(X^c, Y^c) \rangle \\ q_{cz} \ = \ \langle (\sigma_i^z)^2 \rangle = \langle F_2(X^c, Y^c) \rangle \\ r_{cz} \ = \ \langle (\sigma_i^z)^3 \rangle = \langle F_3(X^c, Y^c) \rangle \end{cases} \tag{7}$$

with :

$$\begin{array}{rcl} (m_{sz})_\alpha & = & \langle \langle G(X_\alpha^s, Y^s) \rangle \rangle = \langle \frac{2sh(\beta(X_\alpha^s))}{2ch(\beta(X_\alpha^s))+exp(-\beta Y_\alpha^s)} \rangle \\ (q_{sz})_\alpha & = & \langle \langle H(X_\alpha^s, Y^s) \rangle \rangle = \langle \frac{2ch(\beta(X_\alpha^s))}{2ch(\beta(X_\alpha^s))+exp(-\beta Y_\alpha^s)} \rangle \\ m_{cz} & = & \langle \langle F_1(X^c, Y^c) \rangle \rangle = \langle \frac{3sh(\frac{3}{2}\beta X^c)+sh(\frac{1}{2}\beta X^c)\times exp(-2\beta Y^c)}{2ch(\frac{3}{2}\beta X^c)+2ch(\frac{1}{2}\beta X^c)\times exp(-2\beta Y^c)} \rangle \\ q_{cz} & = & \langle \langle F_2(X^c, Y^c) \rangle \rangle = \langle \frac{9ch(\frac{3}{2}\beta X^c)+ch(\frac{1}{2}\beta X^c)\times exp(-2\beta Y^c)}{4ch(\frac{3}{2}\beta X^c)+4ch(\frac{1}{2}\beta X^c)\times exp(-2\beta Y^c)} \rangle \\ r_{cz} & = & \langle \langle F_3(X^c, Y^c) \rangle \rangle = \langle \frac{27sh(\frac{3}{2}\beta X^c)+sh(\frac{1}{2}\beta X^c)\times exp(-2\beta Y^c)}{8ch(\frac{3}{2}\beta X^c)+8ch(\frac{1}{2}\beta X^c)\times exp(-2\beta Y^c)} \rangle \end{array} \tag{8}$$

where : $\alpha = (1, 2)$

Spin operators are typically replaced by their thermal averages in the mean-field approximation. However, a significant improvement to the theory arises from recognizing that spin operators only possess a limited number of ground states. As a result,

the average values of the functions G, H, F_1, F_2, F_3 can be expressed as the average of polynomials involving spin operators belonging to neighboring spins [60]. This method is implemented through a combinatorial approach, which accurately incorporates single-site kinematic constraints. Until this stage, the right-hand sides of equations (8) include several spin correlation functions. To carry out thermal averaging of these terms, we adopt the general method outlined in reference [61]. This involves applying the integral representation of the Dirac delta function [60] par.

$$\begin{aligned} m_{sz} &= \int d\omega G(\omega, D_z^s) \tfrac{1}{2\pi} \int dt exp(i\omega t) \prod_j \prod_k \langle exp(itJ_s S^s_{kz}) \rangle \langle exp(itJ_{cs} \sigma^c_{jz}) \rangle \\ m_{cz} &= \int d\omega F_1(\omega, D_z^c) \tfrac{1}{2\pi} \int dt exp(i\omega t) \prod_i \prod_l \langle exp(itJ_c \sigma^c_{iz}) \rangle \langle exp(itJ_{cs} S^s_{lz}) \rangle \end{aligned} \tag{9}$$

where :

$$\begin{cases} q_{sz} &= m_{sz}[G(\omega, D_z^s) \rightarrow H(\omega, D_z^s)] \\ q_{cz} &= m_{cz}[F_1(\omega, D_z^c) \rightarrow F_2(\omega, D_z^c)] \\ r_{cz} &= m_{cz}[F_1(\omega, D_z^c) \rightarrow F_3(\omega, D_z^c)] \end{cases} \tag{10}$$

The expressions of the total magnetization M_T, internal energy E, free energy F and susceptibility χ are respectively given by the following formulas :

$$M_T = \frac{6m_c + 6(m_{s1} + m_{s2})}{18} \tag{11}$$

$$E = \frac{6\langle (H_0^c) \rangle + 6[\langle (H_0^s)_1 \rangle + \langle (H_0^s)_2 \rangle]}{18} \tag{12}$$

$$F = \frac{-T[log(Z_c^{N^c}) + log(Z_{s1}^{N_1^s}) + log(Z_{s2}^{N_2^s})]}{N} \tag{13}$$

with,

$$Z_c = 2[ch(\frac{3}{2}\beta X^c) + ch(\frac{1}{2}\beta X^c) exp(-2\beta Y^c)] \tag{14}$$

$$Z_{s1} = 2ch(\beta X_1^s) exp(\beta Y^s) \tag{15}$$

$$Z_{s2} = 2ch(\beta X_2^s) exp(\beta Y^s) \tag{16}$$

$$\chi = \left(\frac{\delta M_T}{\delta h}\right)_{h=0} = \frac{N(\langle M_T^2 \rangle - \langle M_T \rangle^2)}{T} \tag{17}$$

3. RESULTS AND DISCUSSION

In this section, we examine some important and typical results of the bond-diluted mixed Ising nanotube spin-$\frac{3}{2}$ core and spin-1 shell structure. The magnetic properties (total magnetization, compensation behavior), the thermodynamic functions (magnetic susceptibilities, internal energy, and free energy), and hysteresis behaviors of the mixed spin Ising nanotube are explored for diverse adapted parameters. Furthermore, the behavior of the total magnetization versus the temperature will be examined to express the different types of compensation behavior of the system.

A. The thermal behaviors of magnetizations and thermodynamic functions :

1. *The perfect case,* $p = q = 1$ *:*

In this section, we will discuss the effects of D_c, D_s, R_c, and R_{cs}, on the total magnetizations and thermodynamic functions in the perfect case ($p = q = 1.0$).

Figure 2(a) illustrates the evolution of the total magnetization as a function of temperature, with variations in the uniaxial anisotropy in the core D_c. The compensation behavior is observed for low values of D_c ($D_c = -0.2$ and $D_c = -0.4$) in the magnetization of the N-type system according to Néel's classification [62]. For $D_c = -0.2$, the compensated magnetization reaches its maximum, decreases for $D_c = -0.4$, and disappears from $D_c = -0.6$. Also, we notice that the critical temperature T_c diminishes with D_c. On the other hand, the compensation temperature T_{comp} increases with D_c. This result also demonstrates that the system's multi-state operation, as a weak thermal disruption, can induce an inversion of total magnetization near T_{comp}. The paramagnetic case is obtained at high temperatures, as indicated by the thermal decay of magnetization. From $D_c = -0.6$, the system exhibits P-type behavior, due to the relatively large value of the core spins exchange interaction J_c and the large value of D_c. The presence of these forms of spontaneous magnetization in a cylindrical nanotube is explained by the shape effect in nanomaterials, arising from two reasons. The first is related to the small difference in the spins studied in our case, and the second is that the shell spins exceed those of the core.

Additional physical quantities were analyzed under the same set of chosen parameters. We present the internal energy (Fig.2(b)), where we notice that the variation in critical temperature T_c with respect to D_c is consistent with the magnetization results. We also illustrate the evolution of the susceptibility of the system (Fig.2(c)), where we notice that the peaks correspond perfectly to the phase transition at T_c. The free energy plotted in Fig.2(d) presents a minimum, confirming the system's stability at low temperature. At high temperatures, all free energy curves exhibit linear asymptotic behavior, consistent with the approach to the paramagnetic phase.

Fig.3(a) shows the evolution of total magnetization as a function of temperature with variation of the uniaxial anisotropy in the shell D_s.

We notice a remarkable presence of compensation behavior for different values of D_s ($D_s = 0.5; 1.0; 1.5; 2.0; 2.5$). The compensated magnetization has its maximum for $D_s = 0.5$ and decreases with an increase in D_s. Also, it is clearly observed that the compensation temperature increases with D_s, but regarding the critical temperature, no significant variation is observed. That

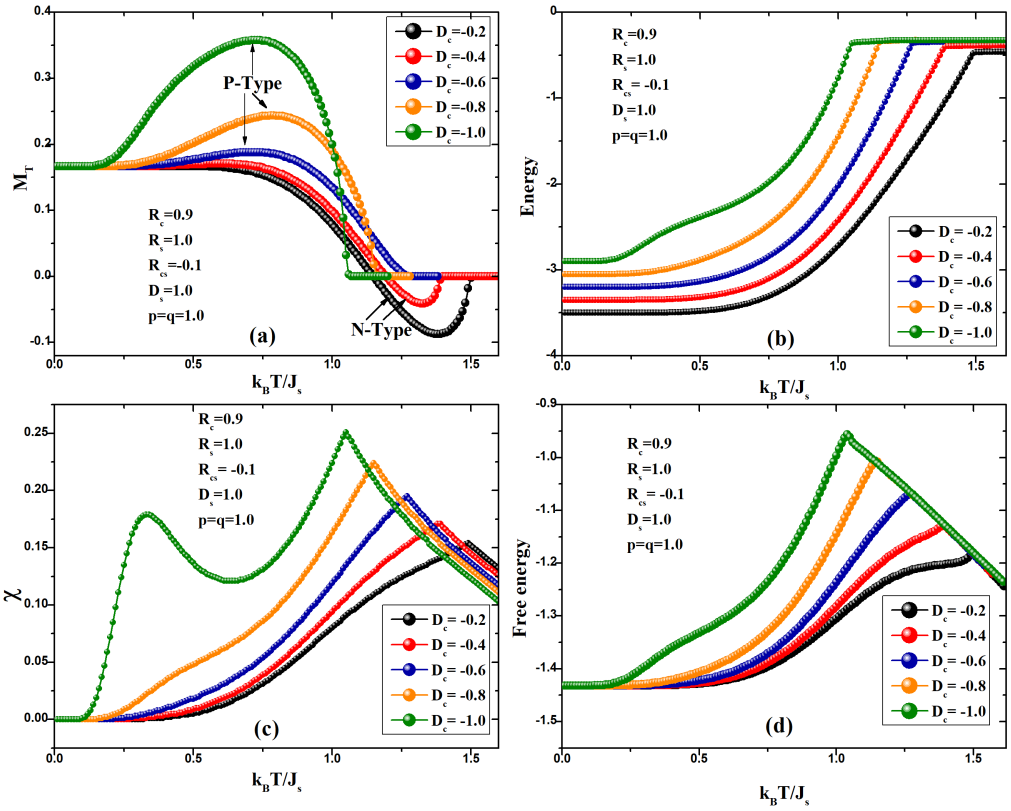

FIG. 2: The total magnetizations (a), internal energy (b), susceptibility (c) and free energy (d) of the system in a presence of compensation behavior are plotted for perfect case which we changed the crystal anisotropy, and we fixed the parameters (R_c; R_s; R_{cs}; D_s; p; q)= (0.9; 1.0; −0.1; 1.0; 1.0; 1.0).

means that the D_s have no remarkable effect on T_c and thus on the system's transition to the paramagnetic phase. For D_s = 3.0, the compensation behavior disappears, and magnetization becomes of P-type. The energetic aspects demonstrate the correspondence between total magnetization and thermodynamic functions, as shown in Fig.3(b), representing internal energy. We observe that at high temperatures, the energy saturates at a negative value with the increase of D_s, due to the presence of quadratic terms of the spin momenta, which becomes more important with larger D_s. These results are very similar to previous studies [63–65]. The system's stability is also indicated by free energy (Fig.3(c)), which represents a minimum at low temperature, for all plotted curves. Furthermore, Fig.3(d) illustrates the evolution of susceptibility, where it increases sharply at low temperatures, showing magnetic ordering. Also, it has two peaks; the first corresponds to a transition from an ordered ferrimagnetic phase to a partially disordered state at a lower temperature. The second peak (at a higher temperature) is usually associated with a complete transition to the paramagnetic phase. The increase in D_s shifts the peaks slightly and reduces the height of the first one, showing how single-ion anisotropy suppresses magnetic order.

Fig.4(a) shows different types of total magnetizations, with varying the core's exchange interaction parameter R_c. For R_c =

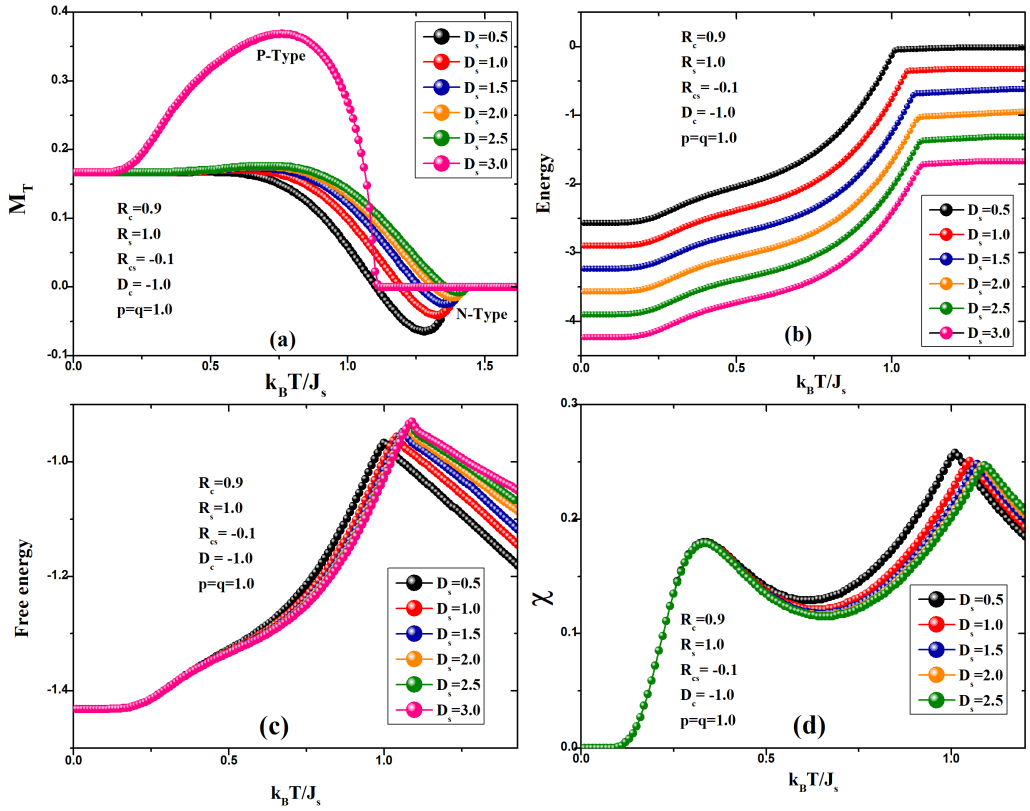

FIG. 3: The total magnetizations (a), internal energy (b), free energy (c) and susceptibility (d) of the system in presence of compensation behavior are plotted for perfect case which we changed the crystal anisotropy D_s, and we fixed the parameters (R_c; R_s; R_{cs}; D_c; p; q)= (0.9; 1.0; −0.1; −1.0; 1.0; 1.0).

0.1, the magnetization is of Q-type, where the sharp drops indicate second-order phase transitions. By increasing the R_c, we find P-type magnetization (for $R_c = 0.3; 0.5; 0.7$). And for $R_c = 0.9$, the compensation phenomenon appears through N-type magnetization, indicating the role of R_c in magnetic interaction strength. Moreover, at low temperatures, the system is magnetically ordered (high magnetization), and at higher temperatures, thermal fluctuations destroy the order. Also, we observe that at $T = 0$, the total magnetization $M_T = 0.5$ for $R_c = 0.1$, and $M_T = 0.167$ for the other values. This result is explained by various transitional states emerging in the core magnetization at low temperature, depending on the exchange interaction R_c. As illustrated in Fig. 4(b), the shell has only Q-type magnetization corresponding to spin state $s = 1$ for all chosen values of R_c. However, associated with spin state $s = 3/2$, the core transitions from Q-type magnetization for $R_c = 0.1$ to S-type magnetization for $R_c = 0.3$, and for $R_c = 0.5; 0.7; 0.9$ it returns to Q-type magnetization. The splitting and merging of the curves show how the sublayers (core and shell) interact and transition at different rates.

In Fig.4(c), the susceptibility shows double peaks, indicating complex magnetic transitions. The first peak exhibits the onset of partial disordering, and the second expresses complete magnetic disorder (paramagnetic state). The internal energy observed in

Fig.4(d) increases progressively with temperature. At low temperatures, energy is minimal (ordered state), it increases as the temperature rises and the system becomes disordered. The kinks in the curves indicate phase transitions. Free energy curves shown in Fig.4(e) reflect the system's stability and phase behavior. Moreover, the changes in curvature or slope correspond to a phase transition. For example, the appearance of a cusp or inflection point indicates a second-order transition.

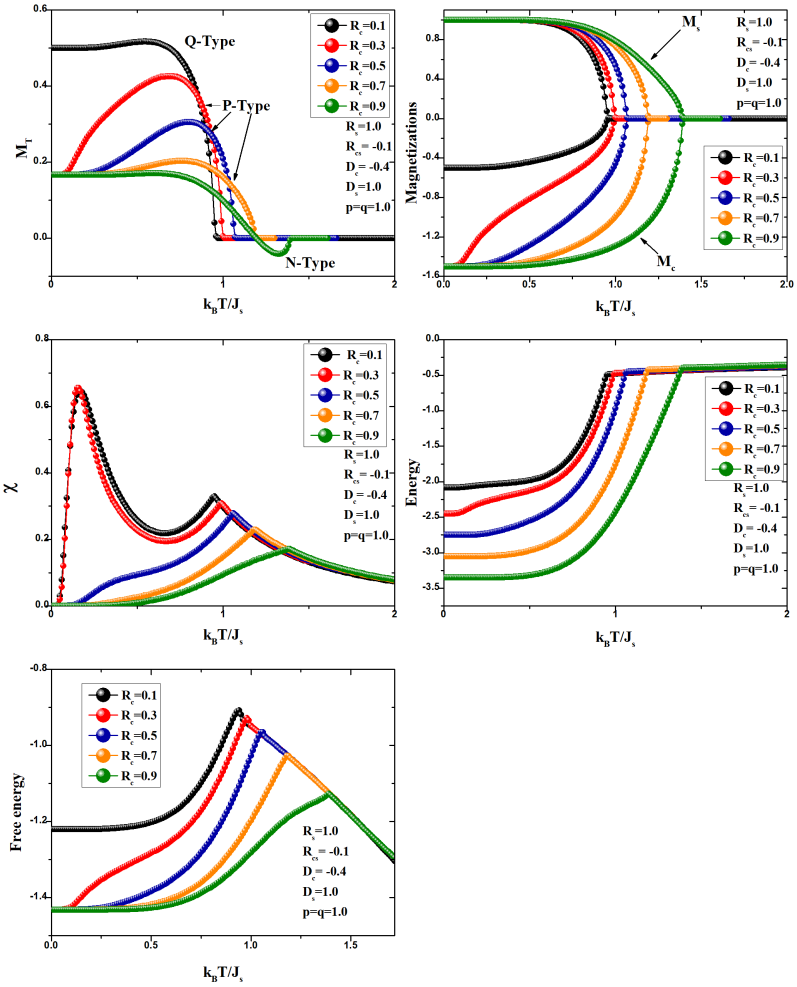

FIG. 4: The total magnetizations (a), the core and shell magnetizations (b), internal energy (c), free energy (d) and susceptibility (e) of the system in presence of compensation behavior are plotted for changed parameter R_c, and fixed parameters (R_s; R_{cs}; D_c; D_s; p; q)= (1.0; −0.1; −0.4; 1.0; 1.0; 1.0).

Fig.5(a) shows the temperature variation of total magnetization for which there is the compensation behavior for a couple of options of the coupling parameters $R_{cs} = 0.1, 0.2, 0.3, 0.4$. This type of behavior is typical for N-type magnetization. The highest level of compensated magnetization occurs at $R_{cs} = 0.1$ and decreases monotonically as the absolute value of R_{cs} increases,

i.e., as exchange interactions become weaker. Total magnetization changes indicate the compensation temperature (T_{comp}) due to an imbalance in exchange coupling. This results in various thermal properties in the sublattice magnetizations, forming the compensation effect with the characteristic relation $M_s(T_{comp}) + M_c(T_{comp}) = 0$.

For $R_{cs} = 0.5$, the compensation behavior disappears, and the system exhibits R-type magnetization according to Strečka classification [66]. Critical temperature is established as the point at which total magnetization rises with the rise in R_{cs}, signifying the onset of the paramagnetic phase. The system remains ferrimagnetic as R_{cs} rises. This is an indication that the ferrimagnetic spin configuration remains controlled by exchange interactions, as indicated in previous studies [18, 67].

For the adapted values of R_{cs} shown in Fig.5, the energy increases with temperature. At high temperatures, the energy saturates at a negative value due to the presence of quadratic terms of the spins' momenta. These results are very similar to previous studies [68–70] and a study on the size effects of a pair of frustrated double-walled nanotubes, see [71].

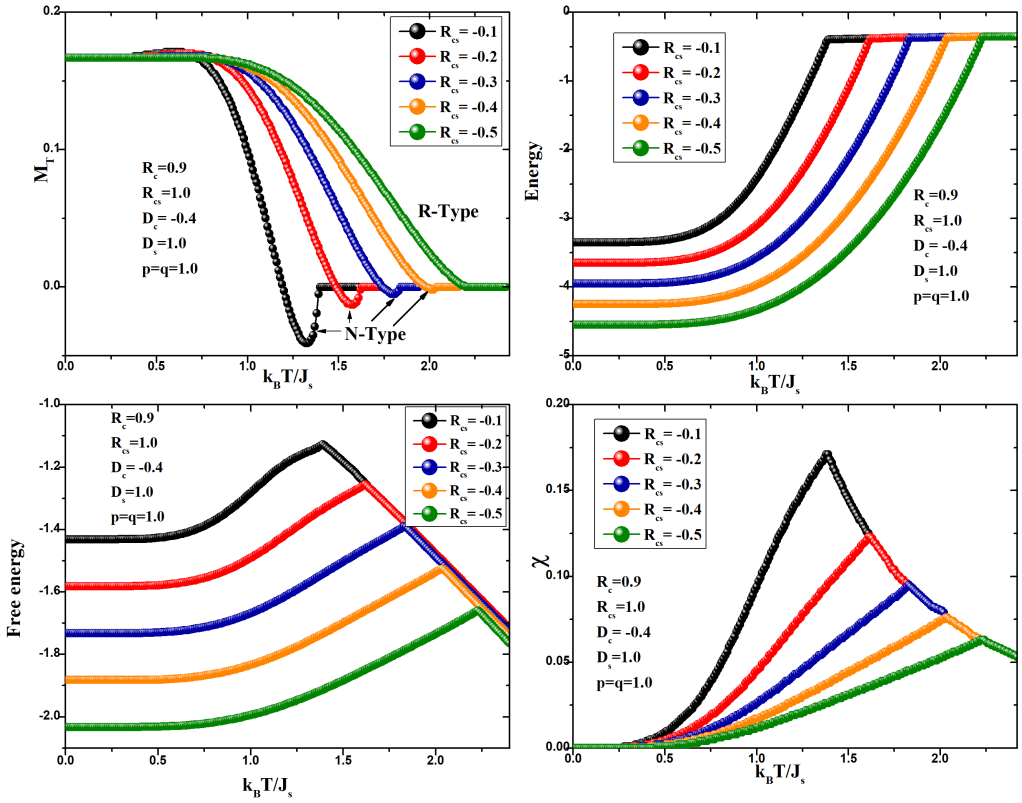

FIG. 5: The total magnetizations (a), internal energy (b), free energy (c) and susceptibility (d) of the system are plotted in a presence of compensation behavior for changed parameter R_{cs}, and fixed parameters (R_c; R_s; D_c; D_s; p; q)= (0.9; 1.0; −0.4; 1.0; 1.0; 1.0).

2. *The diluted case,* $p = 0.8$ *and* $q = 0.2$ *:*

Fig.6(a) illustrates the evolution of total magnetization as a function of temperature with the existence of dilution in both the core ($p = 0.8$) and the shell ($q = 0.2$), but it is most important in the shell. We observe the presence of compensation behavior, through the N-Type magnetization, for all the values of D_c chosen, which is maximal for $D_c = -0.2$, and it vanishes with D_c. This is because a stronger anisotropy favors spin alignment in the easy axis direction. With respect to the temperatures, the compensation temperature increases with D_c but the critical temperature decreases.

On the other hand, Fig.6(b) also represents the variation of magnetization with positive values of D_c, to compare the results with the first case, where we have negative values. We notice that the compensation behavior is more significant with positive values of D_c than with negative values. In addition, the critical temperature increases with D_c. Then, we can conclude that the variation of the critical temperature depends on the absolute value of the crystal anisotropy D_c.

For energetic aspects, Fig.6(c) represents the internal energy, which is consistent with a second-order transition. Furthermore, larger $\mid D_c \mid$ leads to higher baseline energy, as a stronger anisotropy introduces greater internal spin. The variation of the susceptibility with temperature shows that a peak corresponds to a critical temperature. However, as $\mid D_c \mid$ increases, the peak lowers and shifts right, meaning that stronger anisotropy weakens the system's response to an external magnetic field. This behavior indicates the suppression of collective spin fluctuations due to anisotropy. The free energy curves represented in Fig.6(e) exhibit smooth changes, confirming the second-order phase transition. Moreover, we quote that a higher $\mid D_c \mid$ leads to a higher free energy in the ordered phase, reflecting a greater energy cost to maintain order.

Fig.7(a) shows the effect of the shell's anisotropy $D_s$on the total magnetization in the diluted case, where we observe the compensation behavior for all the values chosen for D_s. As D_s increases from -0.5 to 1.5, the magnetization curve shifts slightly to the right and becomes smoother, indicating weaker magnetic ordering and higher critical temperatures for larger D_s. At low D_s (-0.5), magnetization decreases more sharply, indicating stronger ordering effects at lower temperatures. This result means that the variation of D_s over a positive range shows how increased shell anisotropy D_s suppresses magnetic ordering and delays the phase transition.

Fig.7(b) shows that the energy increases steadily with temperature. Furthermore, a higher anisotropy D_s results in an initial energy, indicating more energetically favorable configurations at low temperatures due to enhanced uniaxial anisotropy. Also, we notice that all curves converge at high temperatures, where thermal fluctuations dominate. The susceptibility plotted in Fig.7(c) exhibits a pronounced peak, which shifts to higher temperatures as D_s increases. The highest peak corresponds to $D_s = -0.5$, confirming a stronger response to external fields at lower D_s. For larger D_s, the peak becomes less sharp, showing a reduction in critical behavior due to stronger anisotropy suppressing fluctuations.

In Fig.7(d), free energy shows a non-monotonic behavior: it first decreases, then increases with temperature. Indeed, lower D_s corresponds to lower free energy at low temperature, suggesting more stable magnetic ordering. Also, the curves show smooth transitions, consistent with second-order phase transitions.

Fig.8(a) shows the evolution of total magnetization with variation of core exchange interaction R_c. The curves represent two types of magnetizations: P-type and N-type, the latter represents a compensation behavior corresponding to the highest value

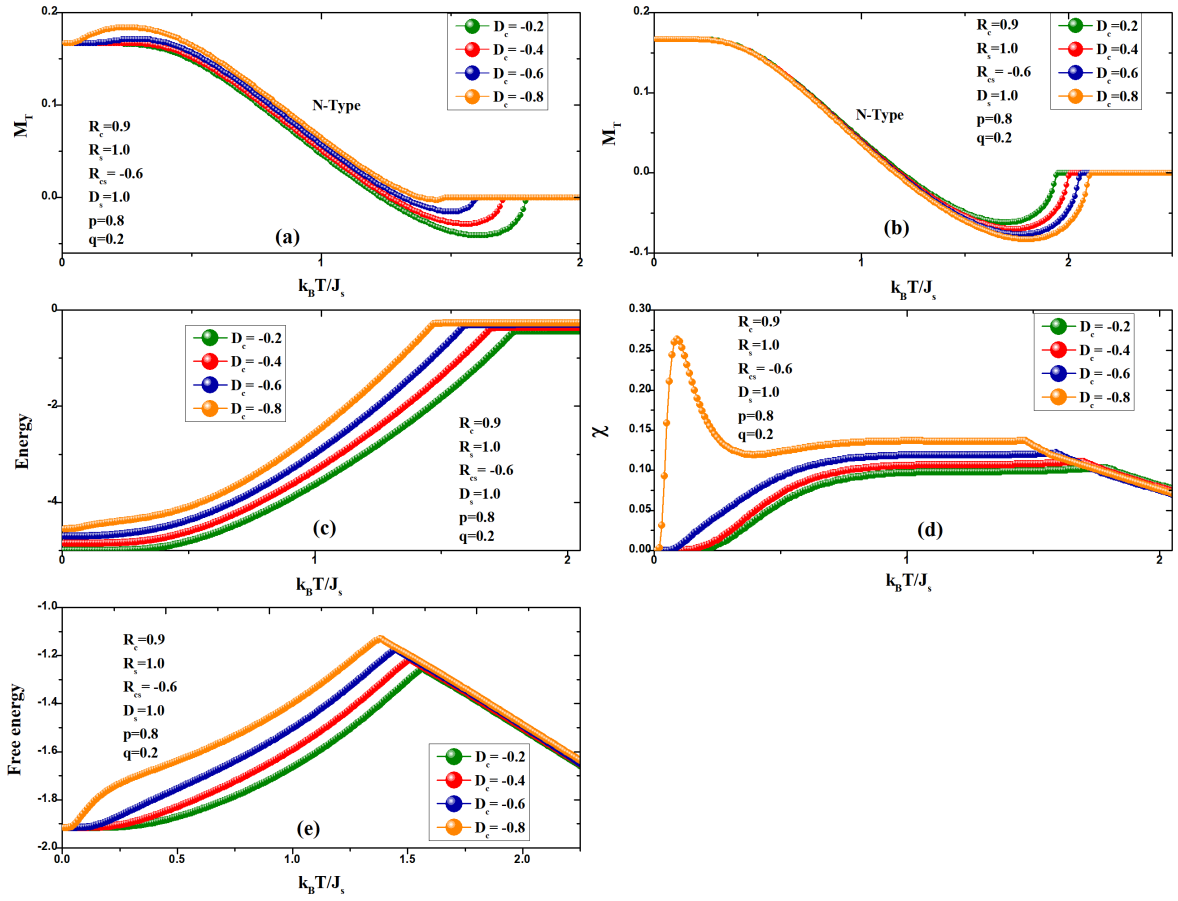

FIG. 6: The total magnetizations (a and b), internal energy (c), susceptibility (d) and free energy (e) of the system are plotted for diluted case which we changed the crystal anisotropy D_c, and we fixed the parameters (R_c; R_s; R_{cs}; D_s; p; q)= (0.9; 1.0; −0.6; 1.0; 0.8; 0.2).

of R_c (R_c = 0.8). This result indicates the role of R_c in magnetic interaction strength, because a stronger negative R_c enhances antiferromagnetic coupling, leading to a faster loss of order with temperature. The paramagnetic case is recovered at high temperatures, as evidenced by the disappearance of the magnetization due to the thermal effect.

The system's energy behavior is depicted in Fig.8(b). We note that a stronger R_c stabilizes lower energy (more ordered) states at very low temperature. This behavior corresponds to the configuration of all spins oriented parallel (the two ferromagnetic layers and antiparallel (the ferrimagnetic case in the interface of the two layers). The stability of the system is also confirmed by the free energy plotted in Fig.8(c), which decreases to a minimum and then increases. Meaning that a stronger R_c deepens the low-temperature free energy, suggesting stronger thermodynamic stability. At high temperatures, curves converge to asymptotic behavior, where entropic contributions dominate.

Fig.8(d) depicts the variation of susceptibility versus temperature. All curves show a clear susceptibility peak. Also, as R_c

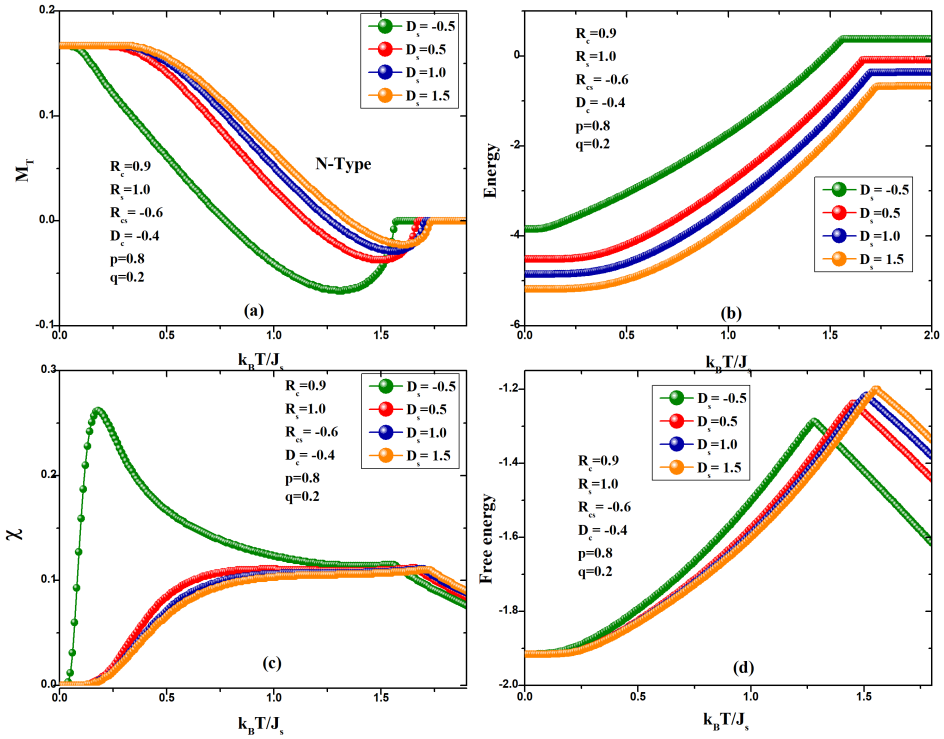

FIG. 7: The total magnetizations (a), internal energy (b), susceptibility (c) and free energy (d) of the system are plotted for diluted case which we changed the crystal anisotropy D_s, and we fixed the parameters (R_c; R_s; R_{cs}; D_c; p; q)= (0.9; 1.0; −0.6; −0.4; 0.8; 0.2).

increases, the peak shifts to lower temperatures, and the height of the peak decreases, indicating a weaker overall response. This result suggests that a stronger R_c suppresses thermal fluctuations in magnetization.

Fig.9(a) illustrates the total magnetization temperature dependence with compensation behavior for specific values of the exchange interaction $R_{cs} = (-0.2; -0.4; -0.6)$ through N-type magnetization. As the temperature increases, M_T drops and crosses zero for all R_{cs}. We also indicate that increasing the magnitude of negative R_{cs} (i.e, making R_{cs} more ferrimagnetic) increases the thermal instability of the system and shifts the compensation point (where $M_T = 0$) to lower temperatures. However, for positive values of $R_{cs} = (0.2; 0.4; 0.6)$ (ferromagnetic case Fig.9(b)), the total magnetization shows a smooth, strictly increasing behavior for all R_{cs} values. No compensation point is obtained, and all magnetizations are typical Q-type. This result is justified by strong sublattice dominance at all temperatures.

The system's energy behavior is depicted in Fig.9(c). We note that the system is stable at very low temperatures, where the energy is minimal. This also matches the arrangement where all spins are aligned either in the same direction (the two ferromagnetic layers) or in the opposite direction (ferrimagnetic case in the interface of the two layers). At high temperatures, the energy saturates at a negative value due to the presence of quadratic terms of the momenta. Our results are consistent with previous theoretical and experimental results [72, 73].

The system's instability is clear in the free energy profile (Fig.9(d)), which systems with more negative R_{cs} show lower free

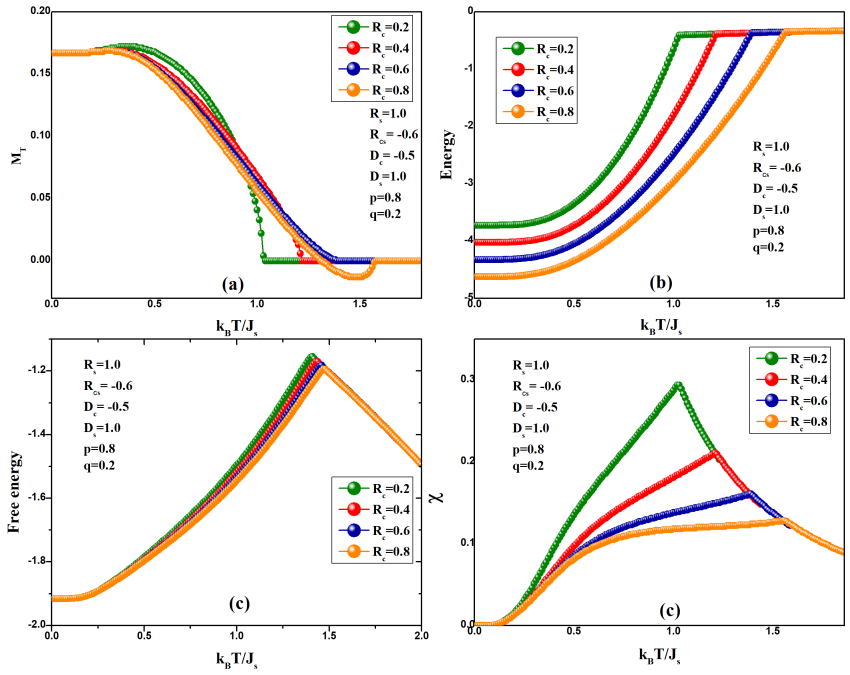

FIG. 8: The total magnetizations (a), internal energy (b), free energy (c) and susceptibility (d) of the system are plotted for changed parameter R_c, and fixed parameters (R_s; R_{cs}; D_c; D_s; p; q)= (1.0; −0.6; −0.5; 1.0 0.8; 0.2).

energy, indicating a more stable ordered state. Furthermore, due to the presence of a compensation temperature T_{comp}, a double peak structure appears in the susceptibility curves. It is important to note that the presence of a compensation temperature improves the performance of the magnetic system and highlights its potential for diverse practical uses.

In Fig. 10, we studied the effects of bond-dilution in the core, the shell, and both, while fixing the other parameters (R_c = 0.9; R_s = 1.0; R_{cs} = −0.6; D_c = −0.3; and D_s = 1.0). Fig.10(a) illustrates the presence of compensation behavior through N-type magnetization for adapted values of parameter q (q = 0.2; 0.4; 0.6; 0.8), which represents the level of disorder in the shell. The compensated magnetization reaches its maximum at q = 0.2, decreases with increasing q, and vanishes at q = 1.0 (the perfect case). However, the core's disorder doesn't present any compensation point (Fig.10(b)), which means that the material is more performant when we dilute the shell's bond. And this result is more supported by Fig.10(c,d,e), where we take various values of p and q.

Fig.11 is plotted for the same values of uniaxial anisotropies D_c and D_s, where in Fig.11(a), D_c and D_s are negative. We notice that as D becomes more negative, the total magnetization shows more pronounced compensation behavior. A clear compensation point (where M_T = 0) exists in several curves through N-type magnetization. This result is due to the increase of single-ion anisotropy, which enhances alignment within sublattices, but also introduces an imbalance in sublattice contributions to M_T, leading to compensation effects. In Fig.11(b), all values of uniaxial anisotropies are positive, implying a hard-axis anisotropy (the system penalizes alignment along a certain direction). The compensation behavior is observed for all chosen values of D.

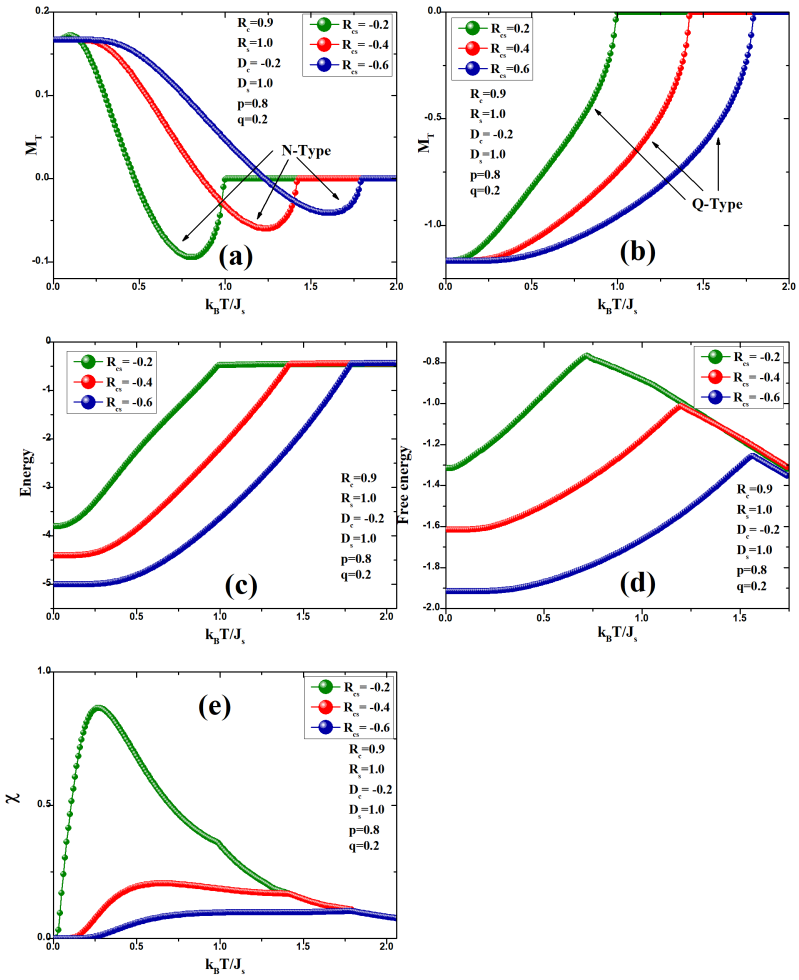

FIG. 9: The total magnetizations (a) (ferrimagnetic case) (b) (ferromagnetic case), internal energy (c), free energy (d) and magnetic susceptibility of the system are plotted for changed parameter R_{cs}, and fixed parameters (R_c; R_s; D_c; D_s; p; q)= (0.9; 1.0; −0.2; 1.0; 0.8; 0.2).

We also indicate the increase of both compensation and critical temperatures with increasing D. This means that a positive alignment makes spin alignment along the preferred axis less favorable, resulting in reduced net magnetization even at low temperatures and weaker long-range order.

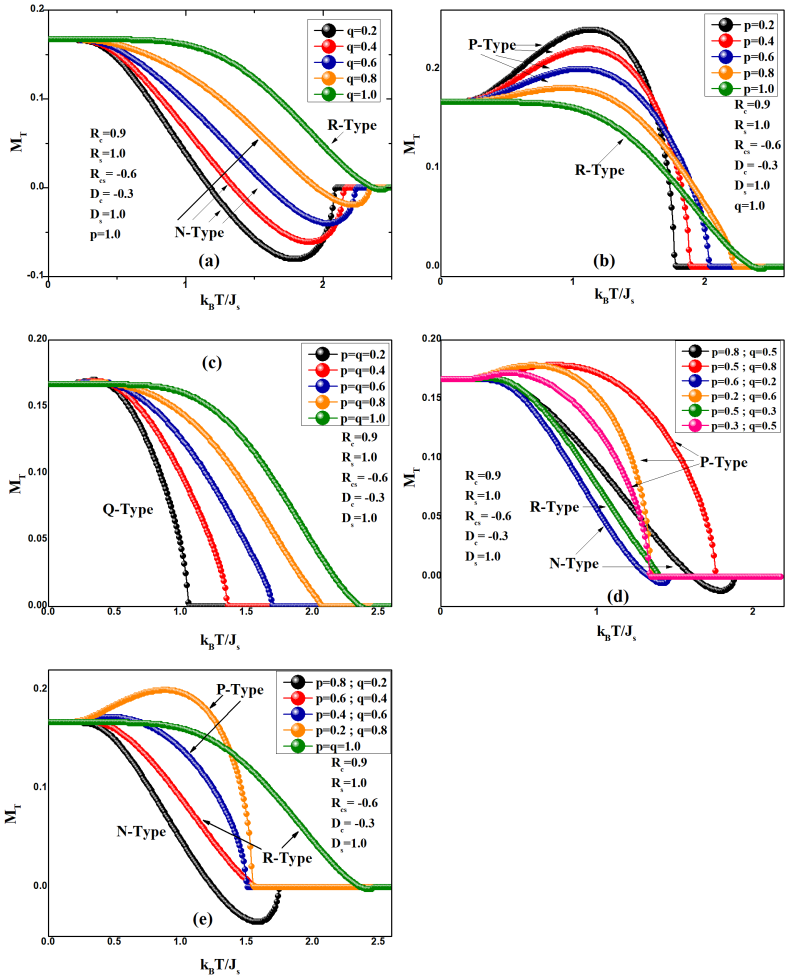

FIG. 10: The total magnetizations of the system are plotted for changed parameters (p, q) and fixed parameters (R_c; R_s; R_{cs}; D_c; D_s)= (0.9; 1.0; −0.6; −0.3; 1.0).

B. Hysteresis behavior :

1. The perfect case, $p = q = 1$:

Fig.12(a-e) investigates the effects of uniaxial anisotropy D_c on the hysteresis behavior of the ferrimagnetic mixed spin nanotube in the ordered case ($p = q = 1.0$). We obtained a series of hysteresis loops with fixed parameters ($R_c = 0.3$; $R_s = 1.0$; $R_{cs} = -0.4$; $D_s = 0.5$ and $T = 0.05$).

In Fig.12(a), we notice that the total system presents quintuple hysteresis loops for $D_c = -0.2$, and curves of total magnetization

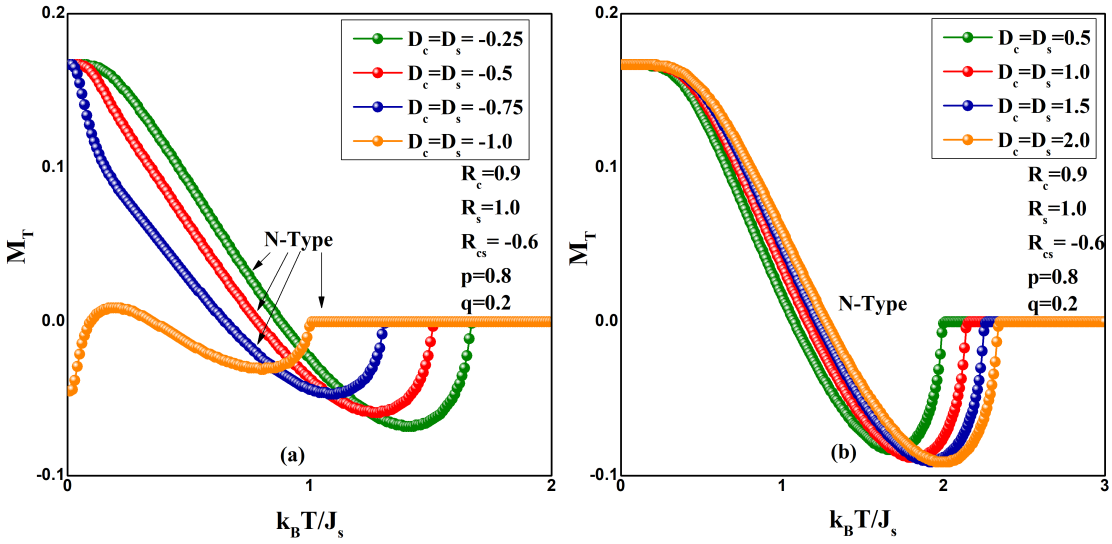

FIG. 11: The total magnetizations of the system are plotted for changed parameters (D_c, D_s) and fixed parameters (R_c; R_s; R_{cs}; p; q)= (0.9; 1.0; −0.6; 0.8; 0.2).

are symmetrical for the positive and negative values of the external magnetic field h. By increasing the longitudinal crystal field of core layers D_c. This interesting phenomenon disappears, and the coercive field decreases. Also, we remark that the influence of D_c on the hysteresis loops of the total system is more important than D_s.

Fig.13(a-d) shows the effects of exchange interactions R_{cs} on the hysteresis loops of the total system for selected values of ($R_{cs} = -0.1; -0.3; -0.5; -0.7$) and with fixed values of ($R_c = 0.3$; $R_s = 1.0$; $D_c = -0.5$; $D_s = 0.5$ and $T = 0.15$). We can observe that the total magnetization curves are symmetrical for positive and negative magnetic field values, and exhibit triple hysteresis loops at exchange coupling $R_{cs} = -0.5$. These multiple hysteresis loop behaviors are due to the competition between the core-shell exchange interactions R_{cs}, the longitudinal crystal field D_c, and the external magnetic field applied to the system. However, the three loops become a single loop at $R_{cs} = -0.7$.

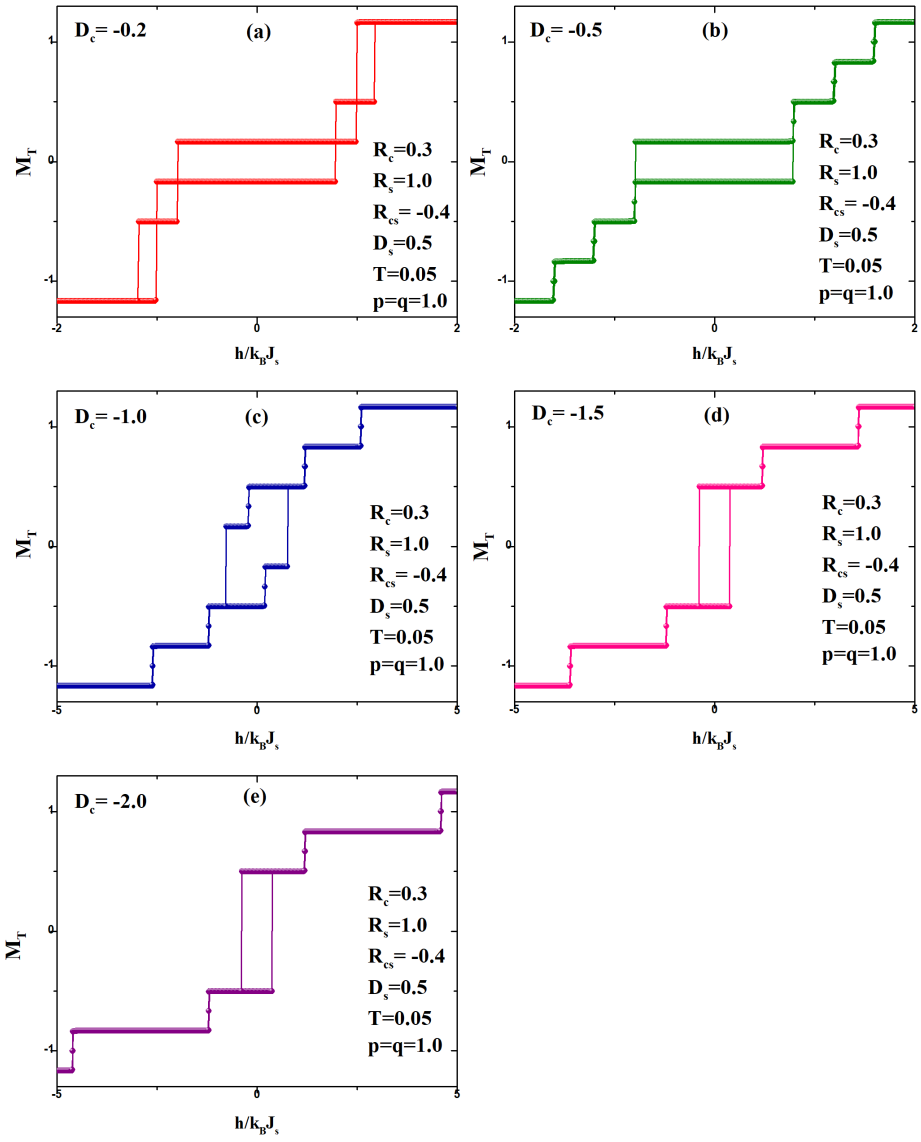

FIG. 12: Hysteresis loops of the system for the fixed parameters $R_c = 0.3$; $R_s = 1.0$; $R_{cs} = -0.4$; $D_s = 0.5$; $T = 0.05$; $p = q = 1.0$; and for different values of the uniaxial anisotropy : (a) $D_c = -0.2$ (b) $D_c = -0.5$ (c) $D_c = -1.0$ (d) $D_c = -1.5$ (e) $D_c = -2.0$.

Fig.14(a-e) illustrates the effects of temperature on the hysteresis loops of the total system with different values of temperature ($T = 0.1; 0.5; 1.0; 1.5; 2.0$) with fixed parameters ($R_c = 0.3$; $R_s = 1.0$; $R_{cs} = -0.5$; $D_c = -0.5$ and $D_s = 0.5$). The system presents triple hysteresis loops at low temperature, and curves of total magnetization are symmetrical for the positive and negative values

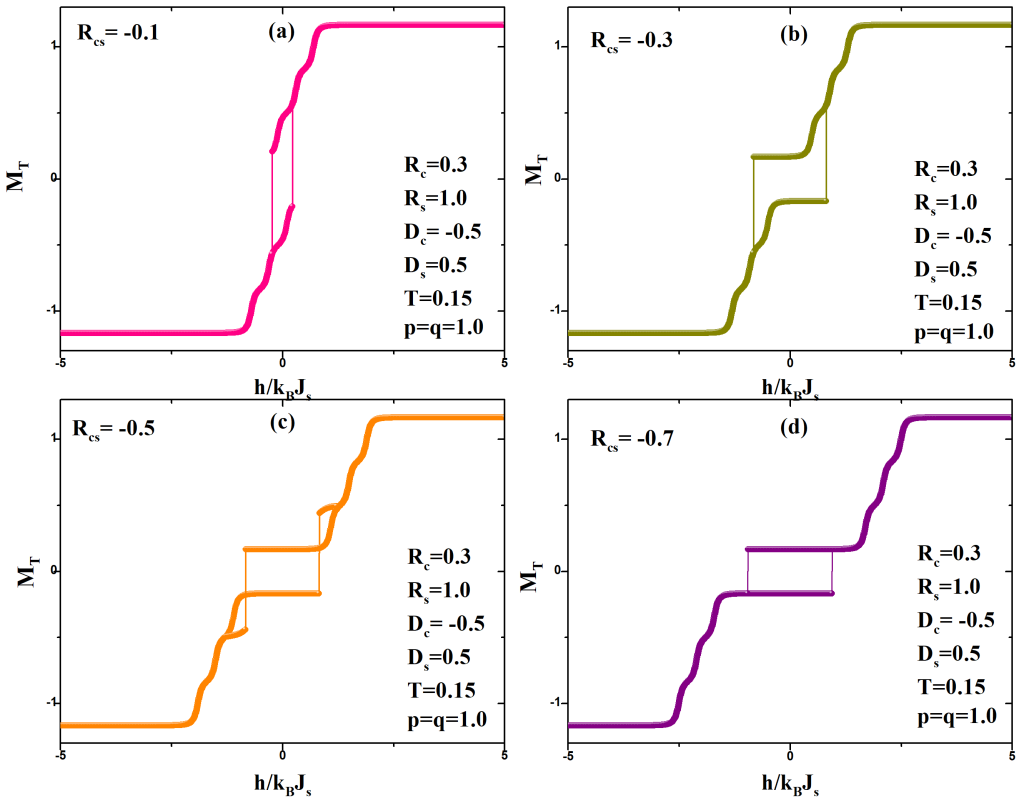

FIG. 13: Hysteresis loops of the system for the fixed parameters $R_c = 0.3$; $R_s = 1.0$; $D_c = -0.5$; $D_s = 0.5$; $T = 0.15$; $p = q = 1.0$; and for different values of the exchange interaction : (a) $R_{cs} = -0.1$ (b) $R_{cs} = -0.3$ (c) $R_{cs} = -0.5$ (d) $R_{cs} = -0.7$.

of the external magnetic field h. By increasing the values of temperature to $T = 2.0$, the number of hysteresis loops disappears progressively, and the coercive field decreases. Furthermore, at high temperatures, the total magnetization curve displays S-type behavior. Similar results have been obtained in previous studies of Ising-type systems such as hexagonal nanoisland [**?**], hexagonal nanowire [**? ?**], nanocube [**?**], cubic nanowire [**?**], nano-graphene [**?**], and molecular-based magnetic materials [**?**].

2. *The diluted case,* $p = 0.2$ *and* $q = 0.8$ *:*

Fig.15(a-e) presents the effects of uniaxial anisotropy of core layers D_c on the hysteresis behavior of the system in a diluted case ($p = 0.2$ and $q = 0.8$), with fixed parameters ($R_c = 0.3$; $R_s = 1.0$; $R_{cs} = -0.4$; $D_s = 0.5$; $T = 0.05$). The curves plotted show single hysteresis loops for selected values of D_c. We observe that the coercive field increases for $D_c = -0.5$ and it decreases when D_c takes larger values. We also notice an increase in remanent magnetization.

This result is mainly due to a stronger uniaxial anisotropy, making it more difficult for spins to flip. And at low temperatures,

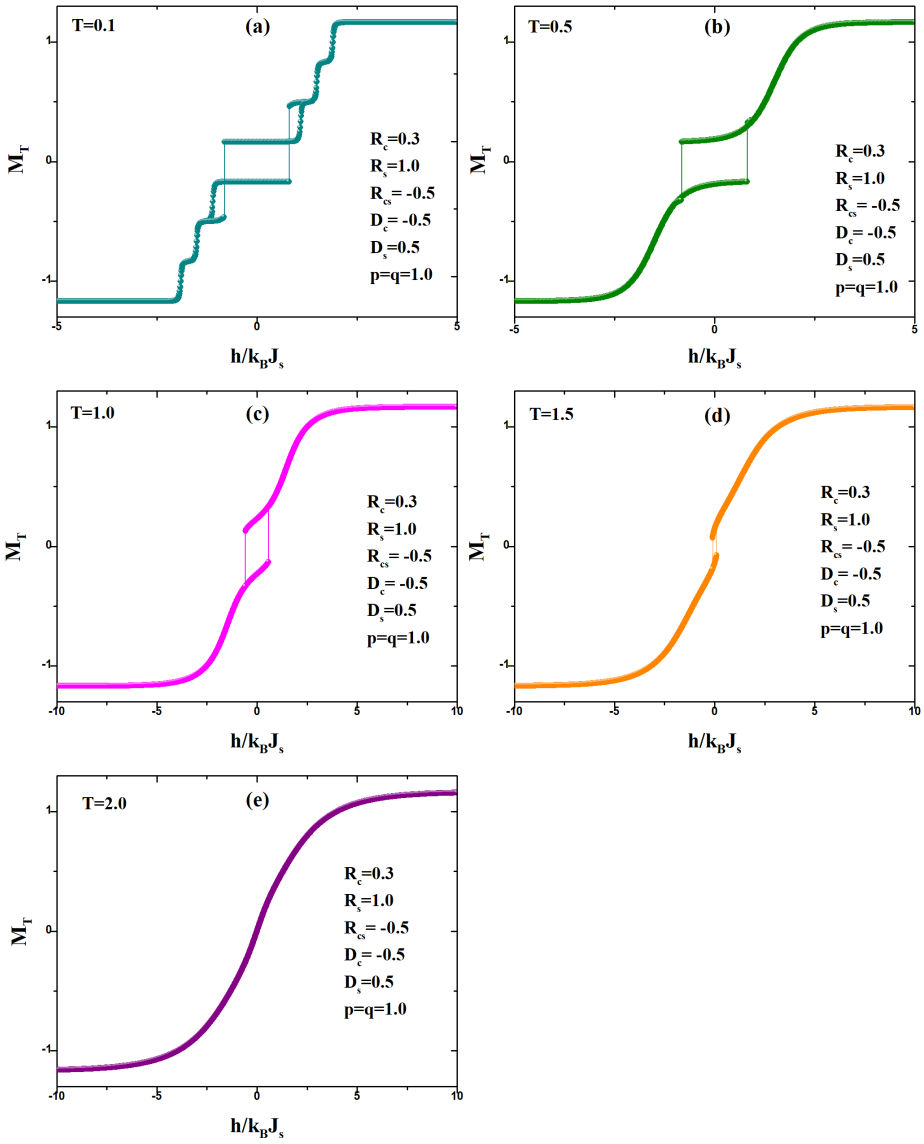

FIG. 14: Hysteresis loops of the system for the fixed parameters $R_c = 0.3$; $R_s = 1.0$; $R_{cs} = -0.5$; $D_c = -0.5$; $D_s = 0.5$; $p = q = 1.0$; and for different values of temperature : (a) $T = 0.1$ (b) $T = 0.5$ (c) $T = 1.0$ (d) $T = 1.5$ (e) $T = 2.0$.

thermal agitation is reduced; therefore, the spins remain aligned more easily. These factors favor a higher remanent magnetization.

On the other hand, we observe a decrease in saturation magnetization because of the dilution, which leads to a decrease in the

density of magnetic moments.

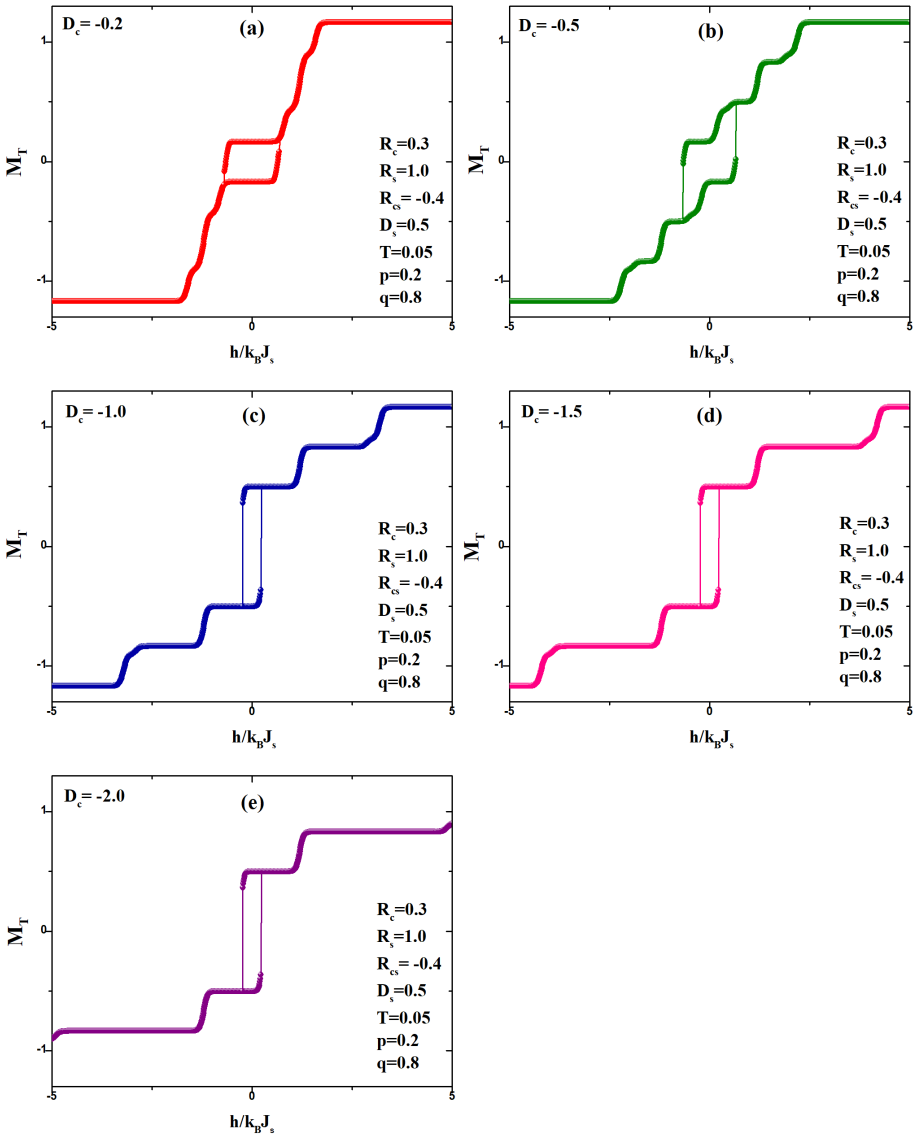

FIG. 15: Hysteresis loops of the system for the fixed parameters $R_c = 0.3$; $R_s = 1.0$; $R_{cs} = -0.4$; $D_s = 0.5$; $T = 0.05$; $p = 0.2$; $q = 0.8$; and for different values of uniaxial anisotropy : (a) $D_c s = -0.2$ (b) $D_c s = -0.5$ (c) $D_c = -1.0$ (d) $D_c = -1.5$ (e) $D_c = -2.0$.

In Fig.16(a-d), we examine the effect of exchange coupling core-shell R_{cs} on the hysteresis curves for selected values of ($R_{cs} = -0.1; -0.3; -0.5; -0.7$) and with fixed values of ($R_c = 0.3$; $R_s = 1.0$; $D_c = -0.5$; $D_s = 0.5$; $T = 0.15$).

For $R_{cs} = -0.1$, no hysteresis loop is observed, and by increasing the exchange coupling R_{cs}, we obtain a single hysteresis loop with a larger coercive field. That means that stronger exchange coupling leads to an increase in the energy barrier.

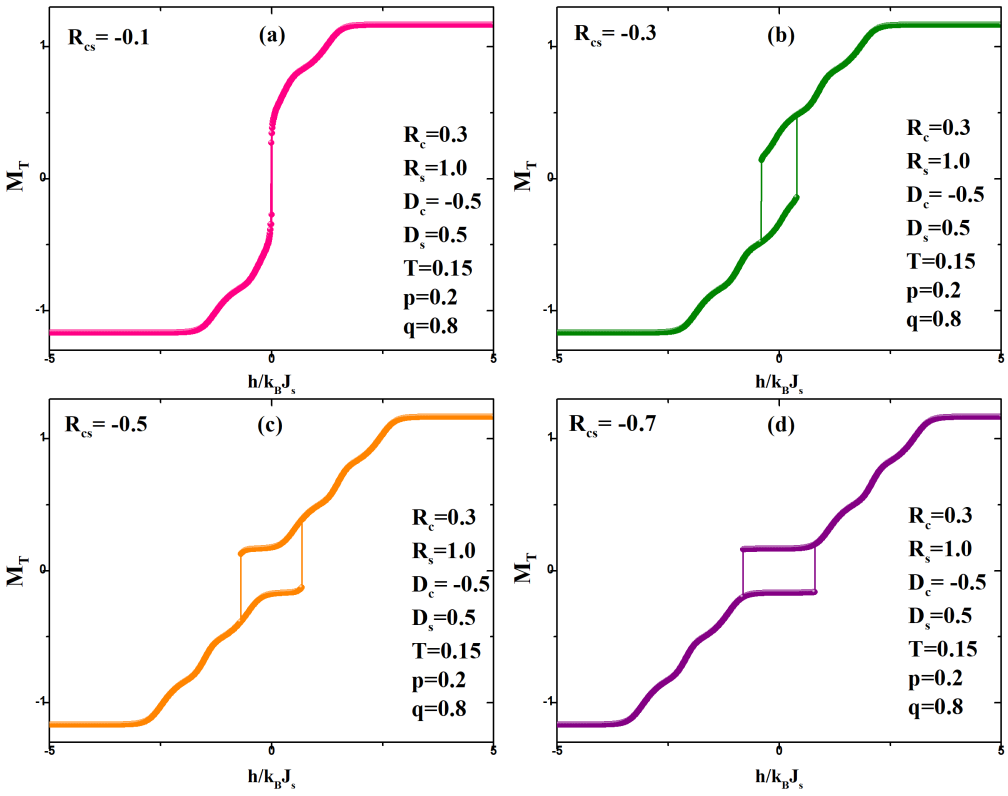

FIG. 16: Hysteresis loops of the system for the fixed parameters $R_c = 0.3$; $R_s = 1.0$; $D_c = -0.5$; $D_s = 0.5$; $T = 0.15$; $p = 0.2$; $q = 0.8$; and for different values of exchange interaction : (a) $R_{cs} = -0.1$ (b) $R_{cs} = -0.3$ (c) $R_{cs} = -0.5$ (d) $R_{cs} = -0.7$.

Fig.17(a-e) shows the effect of temperature on the hysteresis loops in the diluted case ($p = 0.2$ and $q = 0.8$). By increasing the values of temperature, the hysteresis loop becomes more reduced and vanishes for $T = 1.5$.

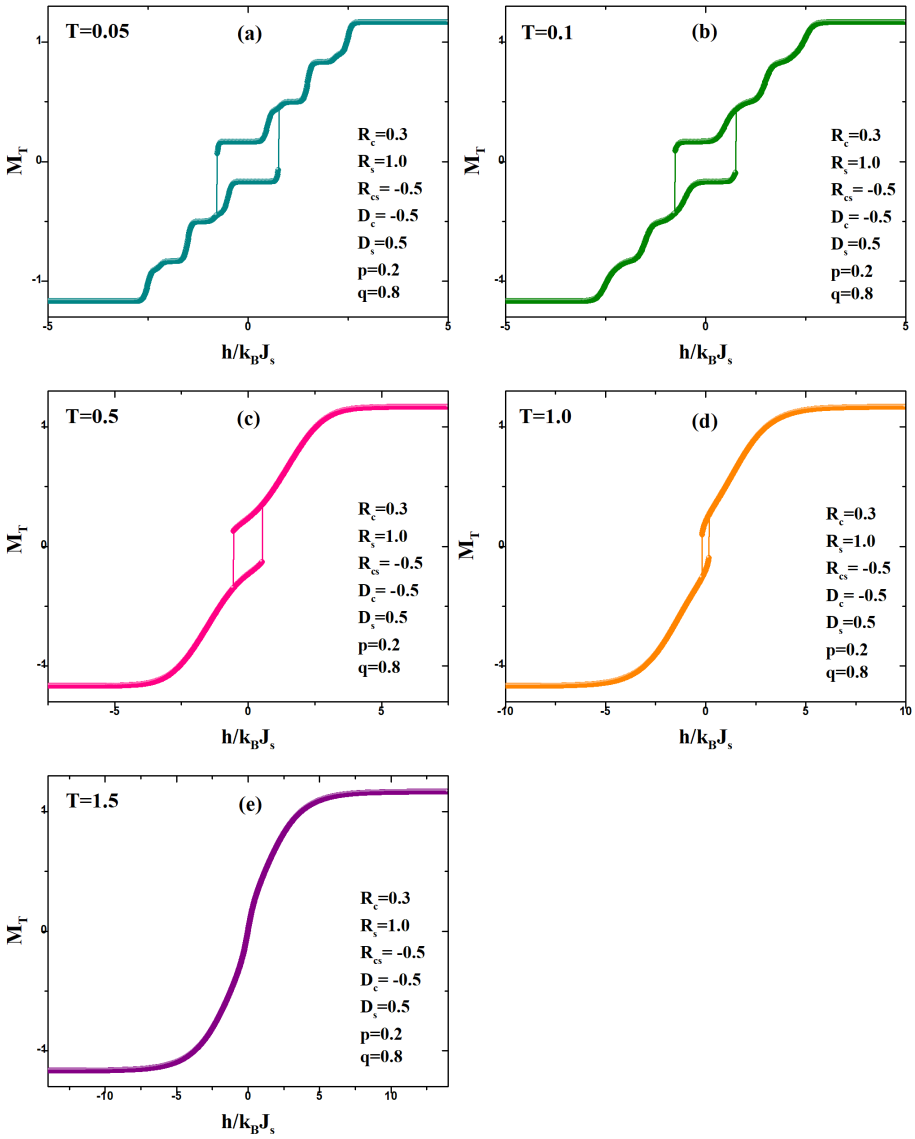

FIG. 17: Hysteresis loops of the system for the fixed parameters $R_c = 0.3$; $R_s = 1.0$; $D_c = -0.5$; $D_s = 0.5$; $T = 0.15$; $p = 0.2$; $q = 0.8$; and for different values of exchange interaction : (a) $R_{cs} = -0.1$ (b) $R_{cs} = -0.3$ (c) $R_{cs} = -0.5$ (d) $R_{cs} = -0.7$.

4. CONCLUSIONS

In this research, we investigated the effect of bond dilution on the magnetic and thermodynamic properties of a core-shell ferrimagnetic Ising nanotube using probability distribution techniques in conjunction with EFT. In addition, we discussed the impact of several parameters, such as crystal anisotropy and exchange interactions, on transition temperatures and compensation behaviors. The energetic behavior was described by internal energy and free energy, which is consistent with other studies on nanostructures [62]. We also examined the evolution of magnetic susceptibility in both the perfect and diluted cases. Finally, the multi-loop hysteresis behavior is studied in detail as a function of various physical parameters of the system. Other projects will be carried out in the same context.

4. ACKNOWLEDGMENTS

The authors would like to acknowledge financial support from the National Centre for Scientific and Technical Research (CNRST)-Morocco.

5. APPENDIX

The probability distributions of the spin states ($S = 1$) and ($\sigma = 3/2$) are as follows:

$$P(S_{iz}) = \frac{1}{2}[((q_s)_\alpha - (m_s)_\alpha)\delta(S+1) + 2(1-(q_s)_\alpha)\delta(S) + ((q_s)_\alpha + (m_s)_\alpha)\delta(S-1)] \tag{18}$$

and :

$$\begin{aligned} P(\sigma_{iz}) = \tfrac{1}{48}[&(-3-2m_c+12q_c+8r_c)\delta(\sigma_{iz}+\tfrac{3}{2}) \\ &+3(9+18m_c-4q_c-8r_c)\delta(\sigma_{iz}+\tfrac{1}{2}) \\ &+3(9-18m_c-4q_c+8r_c)\delta(\sigma_{iz}-\tfrac{1}{2}) \\ &+(-3+2m_c+12q_c-8r_c)\delta(\sigma_{iz}-\tfrac{3}{2})] \end{aligned} \tag{19}$$

Based on equations (9), and by using these probabilities distribution, we obtain the following equations for the longitudinal magnetizations of the layers :

$$m_{cz} = 2^{-N^s}.48^{-N^c} \sum_{\mu_1=0}^{N^c} \sum_{\mu_2=0}^{N^c-\mu_1} \sum_{\mu_3=0}^{N^c-\mu_1-\mu_2} \sum_{k_1=0}^{N^{s,1}} \sum_{k_2=0}^{N^{s,1}-k_1} \sum_{j_1=0}^{N^{s,2}} \sum_{j_2=0}^{N^{s,2}-j_1} C_{\mu_1}^{N^c} C_{\mu_2}^{N^c-\mu_1} C_{\mu_3}^{N^c-\mu_1-\mu_2} C_{k_1}^{N^{s,1}} C_{k_2}^{N^{s,1}-k_1} C_{j_1}^{N^{s,2}} C_{j_2}^{N^{s,2}-j_1}$$
$$(-3 + 2m_c + 12q_c - 8r_c)^{\mu_1} (27 - 54m_c - 12q_c + 24r_c)^{\mu_2} (27 + 54m_c - 12q_c - 24r_c)^{\mu_3}$$
$$(-3 - 2m_c + 12q_c + 8r_c)^{N^c-\mu_1+\mu_2+\mu_3} (q_s^1 - m_s^1)^{k_1} (2(1 - q_s^1))^{k_2} (q_s^1 + m_s^1)^{N^{s,1}-k_1-k_2} (q_s^2 - m_s^2)^{j_1}$$
$$(2(1 - q_s^2))^{j_2} (q_s^2 + m_s^2)^{N^{s,2}-j_1-j_2} F_1[X^c, D_z^c] \tag{20}$$

The equation for the longitudinal quadratic moment q_{cz} (the r_{cz} moment) is obtained by substituting the function F_1 by F_2 (F_3) in the expression of the longitudinal magnetisation of the core:

$$\begin{cases} q_{cz} = m_{cz}[F_1(X^c, D_z^c) \to F_2(X^c, D_z^c)] \\ r_{cz} = m_{cz}[F_1(X^c, D_z^c) \to F_3(X^c, D_z^c)] \end{cases} \tag{21}$$

By the same calculation, we have:

$$(m_{sz})_\alpha = 2^{-N_\alpha^s}.48^{-N_\alpha^c} \sum_{\mu_1=0}^{N_\alpha^c} \sum_{\mu_2=0}^{N_\alpha^c-\mu_1} \sum_{\mu_3=0}^{N_\alpha^c-\mu_1-\mu_2} \sum_{k_1=0}^{N_\alpha^s} \sum_{k_2=0}^{N_\alpha^s-k_1} C_{\mu_1}^{N_\alpha^c} C_{\mu_2}^{N_\alpha^c-\mu_1} C_{\mu_3}^{N_\alpha^c-\mu_1-\mu_2} C_{k_1}^{N_\alpha^s} C_{k_2}^{N_\alpha^s-k_1}$$
$$(-3 + 2m_c + 12q_c - 8r_c)^{\mu_1} (27 - 54m_c - 12q_c + 24r_c)^{\mu_2} (27 + 54m_c - 12q_c - 24r_c)^{\mu_3}$$
$$(-3 - 2m_c + 12q_c + 8r_c)^{N_\alpha^c-(\mu_1+\mu_2+\mu_3)} (q_{s\beta} - m_{s\beta})^{k_1} (2(1 - q_{s\beta}))^{k_2} (q_{s\beta} + m_{s\beta})^{N_\alpha^s-k_1-k_2} G[X_\alpha^s, D_z^s] \tag{22}$$

$$(q_{sz})_\alpha = (m_{sz})_\alpha[G(X_\alpha^s, D_z^s) \to H(X_\alpha^s, D_z^s)] \tag{23}$$

with:

$$X^c = \frac{1}{2} J_{cs} \left[\left(N^{s,1} + N^{s,2} \right) - 2k_1 - k_2 - 2j_1 - j_2 \right] + \frac{1}{2} J_c \left[3N^c - 6\mu_1 - 4\mu_2 - 2\mu_3 \right] \tag{24}$$

$$X_\alpha^s = \frac{1}{2} J_s \left[N_\alpha^s - 2k_1 - k_2 \right] + \frac{1}{2} J_{cs} \left[3N_\alpha^c - 6\mu_1 - 4\mu_2 - 2\mu_3 \right] \tag{25}$$

REFERENCES

[1] S. Iijima, *Nature* **354** 56-58 (1991)

[2] S.J. Tans, A.R.M. Verschueren, C. Dekker, *Nature* **393** 49-52 (1998)

[3] M. Sato, A. Noguchi, N. Demachi, N. Oki, M. Endo, *Science* **264** 556-558 (1994)

[4] A. Cao, D.L. Dickrell, W.G. Sawyer, M.N. Ghasemi-Nejhad, P.M. Ajayan, *Science* **310** 1307-1310 (2005)

[5] P.W. Barone, S. Baik, D.A. Heller, M.S. Strano, *Nat Mater* **4** 86-92 (2005)

[6] D. Pantarotto, J.P. Briand, M. Prato, A. Biancoet, *Chem Commun* **10** 16-17 (2004)

[7] F.G. Kühl, T.J. Kazdal, S. Lang, M.J. Hampe, *Adsorption* **23** 293 (2017)

[8] X.W. Su, F. Jiang, J. Wuhan, *Univ Technol Mater Sci Ed* **30** 959 (2015)

[9] Y.H. Fang, X.T. Tang, X. Sun, Y.F. Zhang, J.W. Zhao, L.M. Yu, Y. Liu, X.L. Zhao, *J Appl Phys* **121** 224301 (2017)

[10] Z.L. Wang, H.Y. Zhang, H.W. Cao, L.C. Wang, Z.Y. Wan, Y.F. Hao, X.T. Wang, *Int J Hydrogen Energy* **42** 17394 (2017)

[11] K.K. Rani, R. Devasenathipathy, S.F. Wang, C. Yang, *Ionics* **23** 3219 (2017)

[12] J.F. Ye, H.J. Zhang, R. Yang, X.G. Li, L.M. Qi, *Small* **6** 296 (2010)

[13] Z.D. Cai, L.H. Wen, F.S. Li, *Chin J Chem Phys* **20** 821 (2007)

[14] Y. Al Qahoom, K. El Kihel, R. Aharrouch, A. Al-Rajhi, M. Madani and M. El Bouziani, *Journal of Nano Research* **81** 85-103 (2023)

[15] B. Nmaila, A. Kadiri, A. Arbaoui, L.B. Drissi, R. Ahl Laamara, K. Htoutou, *Chinese Journal of Physics* **79** 362-373 (2022)

[16] N. Maaouni, Z. Fadil, A. Mhirech, B. Kabouchi, L. Bahmad, W. Ousi Benomar, *Solid State Communications* **321** 114047 (2020)

[17] Y. Liu, W. Wang, D. Lv, X. Zhao, T. Huang, Z. Wang, *Physica B: Condensed Matter* **541** 79-88 (2018)

[18] A Arbaoui, K Htoutou, L B Drissi and R. Ahl Laamara, *J Supercond Nov Magn* **34** 3413–3423 (2021)

[19] K Htoutou and A Arbaoui, *Physica. B* **643** 414095 (2022)

[20] A. Arbaoui, R. Ahl Laamara, L.B. Drissi, K. Htoutou, *J of Magn and Magn Mater* **584** 171070 (2023)

[21] W. Wang, Y. Liu, Z. Gao, X. Zhao, Y. Yang and S. Yang, *Physica E* **101** 110–124 (2018)

[22] M. Gharaibeh, S. Alqaiem, A. Obeidat, A. Al-Qawasmeh, S. Abedrabbo and M. H. A. Badarneh, *Physica A* **584** 126394 (2021)

[23] R. Allen and G. Connell, *J Appl Phys* **53** 2353-2355 (1982)

[24] C. Savage, F. Marquis, M. Watson and P. Meystre, *Appl Phys Lett* **52** 1277-1278 (1988)

[25] T. Kaneyoshi, *J Appl Phys* **64** 2545 (1988)

[26] T. Kaneyoshi, *Phys. Status Solidi B* **248** 250 (2011)

[27] T. Kaneyoshi, *Phys. Section A: Stat. Mech. Appl* **390** 3697 (2011)

[28] T. Kaneyoshi, *Solid State Commun* **151** 1528 (2011)

[29] W. Wang, W. Jiang and D. Lv, *Phys. Stat. Solidi b* **249** 190 (2012)

[30] N. Hachem, Y. Al Qahoom, A. Aharroch, M. Madani, M. El Bouziani, *Romanian Journal of Physics* **67** 612 (2022)

[31] M. Keskin, N. Sarli and B. Deviren, *Solid State Commun* **151** 1025 (2011)

[32] S. Bouhou, I. Essaoudi, A. Ainane, A. Oubelkacem, R. Ahuja and F. Dujardin, *J. Supercond. Novel Magn* **28** 885 (2015)

[33] L. Darbali, B. Nmaila, L. B. Drissi, R. Ahl Laamara and K. Htoutou, *Indian J Phys* 1-16 (2025), https://doi.org/10.1007/s12648-025-03658-1

[34] W. Jiang, V. Cheong Lo, B. D. Bai and J. Yang, *Physica A* **389** 2227 (2010)

[35] S. Bouhou, I. Essaoudi, A. Ainane, M. Saber, F. Dujardin and J. J. de Miguel, *J. Magn. Magn. Mater* **324** 2434 (2012)

[36] K. Htoutou, B. Nmaila, M. Madani, L.B. Drissi and R. Ahllaamara, *Mater Res Express* **4** (11) 116108 (2017)

[37] Z.D. Vatansever, *J. Alloys Compd* **720** 388–394 (2017)

[38] Y. Kocakaplan and E. Kantar, *Eur. Phys. J. B* **87** (6) 135 (2014)

[39] W. Jiang and J.Q. Huang, *Physica E* **78** 115–122 (2016)

[40] M. Yang, W. Wang, B.C. Li, H.J. Wu, S.Q. Yang and J. Yang, *Physica A* **539** 122932 (2020)

[41] B.Z. Mi, C.J. Feng, J.G. Luo and D.Z. Hu, *Superlattices Microstruct* **113** 524–533 (2018)

[42] N. De La Espriellaa and G.M. Buendia, *Physica A* **389** (14) 2725–2732 (2010)

[43] N. De La Espriellaa, C.O. Lopez and F.T. Hoyos, *Rev. Mexicana Fís* **59** (2) 95–101 (2013)

[44] K. Htoutou, Y. Benhouria, A. Oubelkacem, R.A. Laamara and L.B. Drissi, *Chin. Phys. B* **26** (12) 127501 (2017)

[45] Y. Kocakaplan, E. Kantar and M. Keskin, *Eur. Phys. J. B* **86** (10) 420 (2013)

[46] R.M. Francisco and J.P. Santos, *Phys. Lett. A* **383** (11) 1092–1098 (2019)

[47] Z. Jie, X.X. Guang and W.G. Zhu, *Commun. Theor. Phys* **52** (1) 163 (2009)

[48] A. Patsopoulos and D. Kechrakos, *J. Magn. Magn. Mater* **465** 678–684 (2018)

[49] W. Wang, D. Lv, F. Zhang, J. l. Bi and J.N. Chen, *J. Magn. Magn. Mater* **385** 16–26 (2015)

[50] M. Ertas and Y. Kocakaplan, *Phys. Lett. A* **378** (10) 845–850 (2014)

[51] H.K. Mohamad and H.F. Alturki, *J. Supercond. Nov. Magn* **32** (12) 3971–3978 (2019)

[52] M. Ertas and A. Yilmaz, *Comput. Condens. Matter* **14** 1–7 (2018)

[53] K. Yao, J. Li, Z. Liu, H. Fu and L. Zu, *Commun. Theor. Phys* **47** (4) 741 (2007)

[54] J.Y. Chen, N. Ahmad, D.W. Shi, W.P. Zhou, X.F. Han, *J. Appl. Phys* **110** 073912 (2011)

[55] Q. Xu, Z.J. Wang, Y.G. Wang, H.Y. Sun, *J. Magn. Magn. Mater* **419** 166 (2016)

[56] W. Jiang, X.X. Li, A.B. Guo, H.Y. Guan, Z. Wang, K. Wang, *J. Magn. Magn. Mater* **355** 309 (2014)

[57] A. Arbaoui, R. Ahl Laamara, L.B. Drissi and K. Htoutou, *J of Magn and Magn Mater* **584** 171070 (2023)

[58] Y. Benhouria, A. Oubelkacem, I. Essaoudi, A. Ainane and R. Ahuja, *J. Supercond. Nov. Magnetism* **30** 839 (2017)

[59] J.Y. Liang, C.L. Zou, W. Jiang and X.X. Li, *Physica E* **69** 81 (2015)

[60] K Htoutou, A Oubelkacem, Y Benhouria, I Essaoudi, A Ainane and R Ahuja, *J Supercond Nov Magn* **30** 1247-1256 (2017)

[61] J. W. Tucker, M. Saber and L. Peliti, *Physica A* **206** 497 (1994)

[62] L. Néél, *Ann Physics* **3** 137 (1948)

[63] K. El Kihel, R. Aharrouch, Y. Al Qahoom, M. Madani, N. Hachem and M. El Bouziani, *Multidiscip Model Mater Struct* **17** 615-629 (2021)

[64] T. Mouhrach, K. El Kihel, M. Salama, A. Fathi, K. Sbiaai and M. El Bouziani, *J Magn Magn Mater* **580** 170932 (2023)

[65] W. Jiang, X. X. Li, A. B. Guo, H. Y. Guan, Z. Wang and K. Wang, *J Magn Magn Mater* **355** 309-318 (2014)

[66] J. Strecka, *Physica A* **360** 379 (2006)

[67] K. Htoutou and A. Arbaoui, *Physica B* **643** 414095 (2022)

[68] Y. Liu, W. Lv, D. Wang, X.R. Zhao, T. Huang and Z.Y. Wang, *Physica B* **541** 79–88 (2018)

[69] M. Boughrara, M. Kerouad and A. Zaim, *J Magn Magn Mater* **360** 222–228 (2014)

[70] Y. Benhouria, B. Lamarti, A. Oubelkacem, I. Essaoudi, A. Ainane and R. Ahuja, *J Supercond Nov Magn* **33** (3) 817–824 (2020)

[71] Z. Liu and H. Ian, *J Supercond Nov Magn* **31** 2411–2419 (2018)

[72] H. Gao, T. Zhang, Y. Zhang, Y. Chen, B. Liu, J. Wu, X. Liu, Y. Li, M. Peng, Y. Zhang, G. Xie, F. Zhao and H.M. Fan, *J Mater Chem B* **8** (3) 515–522 (2020)

[73] N. Alon, T. Havdala, H. Skaat, K. Baranes, M. Marcus, I. Levy, S. Margel, A. Sharoni and O. Shefi, *Lab A Chip* **15** (9) 2030–2036 (2015)

[74] W. Wang, Z. Peng, S.S. Lin, Q. Li, D. Lv and S. Yang, *Superlattices Microstruct* **113** 178–193 (2018)

[75] D. Lv, W. Jiang, Y. Ma, Z. Gao and F. Wang, *Physica E* **106** 101–113 (2019)

[76] M. El Hamri, S. Bouhou, I. Essaoudi, A. Ainane and R. Ahuja, *J. Magn. Magn. Mater* **413** 30–38 (2016)

[77] W. Jiang, V.C. Lo, B.D. Bai and J. Yang, *Physica A* **389** (11) 2227–2233 (2010)

[78] Y. Benhouria, I. Bouziani, I. Essaoudi, A. Ainane and R. Ahuja, *J. Magn. Magn. Mater.* **460** 223–228 (2018)

[79] W. Jiang, V.C. Lo, B.D. Bai and J. Yang, *Physica A* **389** (11) 2227–2233 (2010)